

ACCRETION ONTO THE COMPANION OF ETA CARINAE DURING THE SPECTROSCOPIC EVENT: II. X-RAY EMISSION CYCLE

Muhammad Akashi, Noam Soker, Ehud Behar

*Department of Physics, Technion—Israel Institute of Technology, Haifa 32000 Israel;
akashi@techunix.technion.ac.il; soker@physics.technion.ac.il; behar@physics.technion.ac.il.*

ABSTRACT

We calculate the X-ray luminosity and light curve for the stellar binary system η Car for the entire orbital period of 5.54 years. By using a new approach we find, as suggested before, that the collision of the winds blown by the two stars can explain the X-ray emission and temporal behavior. Most X-ray emission in the 2 – 10 keV band results from the shocked secondary stellar wind. The observed rise in X-ray luminosity just before minimum is due to increase in density and subsequent decrease in radiative cooling time of the shocked fast secondary wind. Absorption, particularly of the soft X-rays from the primary wind, increases as the system approaches periastron and the shocks are produced deep inside the primary wind. However, absorption can not account for the drastic X-ray minimum. The 70 day minimum is assumed to result from the collapse of the collision region of the two winds onto the secondary star. This process is assumed to shut down the secondary wind, hence the main X-ray source. We show that this assumption provides a phenomenological description of the X-ray behavior around the minimum.

Subject headings: binaries: close—circumstellar matter—stars: individual: η Carinae—stars: mass loss—stars: winds

1. INTRODUCTION

The X-ray light curve of η Carinae has a period of 5.54 years with a deep, non-zero minimum of ~ 70 days (Corcoran 2005) every period. Some variability is observed during

the minimum (Hamaguchi et al. 2005). The minimum is more or less coincidental with the fading of many visible emission lines and a decline in the IR. It is widely accepted that η Car is a binary system (e.g. Daminieli 1996; Daminieli et al. 1997, 2000; Ishibashi et al. 1999; Corcoran et al. 2001a,b; 2004b; Pittard & Corcoran 2002; Duncan & White 2003; Fernandez Lajus et al. 2003; Smith et al. 2004; Whitelock et al. 2004; Steiner & Daminieli 2004; Verner et al. 2005; Iping et al. 2005), and we refer to it as such. The more massive companion of the η Car binary system (the one that caused the Great Eruption of ~ 1840 ; see description of the eruption in Davidson & Humphreys 1997) will be referred to here as the primary, while the companion, probably an O-type star (Verner et al. 2005), will be referred to as the secondary. The aforementioned periodic brightness minima are believed to occur near periastron passage and are generally termed the spectroscopic event (e.g., Daminieli et al. 2000).

Corcoran et al. (2001a) and Pittard & Corcoran (2002) demonstrated that the collision of the winds blown by the two stars can account for the X-ray light curve. However, they had problems in accounting for the X-ray minimum. The X-ray properties of η Car are reviewed in section 2.1. In examining the properties of the colliding winds of the two stars, Soker (2005a, b) has suggested that for several weeks near periastron passages the secondary accretes mass from the primary. This suggestion of accretion is motivated by observations, which show accretion from winds in many other types of binary systems, e.g., symbiotic systems (e.g., Skopal 2005), and from numerical simulations showing the likelihood of accretion from a wind (e.g., Jahanara, et al. 2005), where in some cases an accretion disk is formed (Mitsumoto et al. 2005). This accretion, Soker suggested, shuts down the secondary’s wind, hence the X-ray emission, leading to the X-ray minimum. This scenario is described in section 2.2. However, Soker did not explore the X-ray light curve around the minimum. This is the subject of the present paper. In §3 the X-ray emission of the colliding winds is examined. The X-ray emission during the accretion phase is examined in §4. Our discussion, where the model for the X-ray minimum is summarized according to the results of §3 and 4, is presented in §5.

2. X-RAY MINIMUM

2.1. Observed X-Ray Minimum

The main relevant properties of the X-ray emission near the minimum are as follows.

(1) *Minimum.* The X-ray emission of η Car between 2 and 10 keV is normally at a level of 4×10^{34} erg s $^{-1}$. This emission is believed to result from the collision of the two winds from

the two stars (Corcoran et al. 2001a; Pittard & Corcoran 2002), as in similar massive binary systems (Usov 1992), most notably the WR-O binary system WR 140 (Williams et al. 1990). There is an almost flat minimum in the X-ray emission of η Car, lasting ~ 70 days (0.035 of the cycle) (Ishibashi et al. 1999; Corcoran et al. 2001a; Corcoran et al. 2004b; Corcoran 2005). The interacting massive binary system WR 140 shows a similar X-ray light curve to that of η Car, but the minimum is very short and not as flat. Hence, it can be explained by absorption of the X-rays by the dense wind of the WR star (Corcoran et al. 2004b; Pollock et al. 2005). Conversely, in η Car the X-ray minimum is almost flat and appears to be a reduction in observed X-ray emission measure, which is difficult to explain by absorption alone (Ishibashi et al. 2003; Hamaguchi et al. 2005)

(2) *Behavior prior to minimum.* The X-ray intensity increases prior to the start of the X-ray minimum and then drops sharply to minimum (Corcoran 2005). In this paper, phases are measured from periastron passage, which may or may not be the same as the start of the X-ray minimum (Martin et al. 2005). The decline starts before the maximum of the He II λ 4686Å line (Martin et al. 2005) and the maximum of the IR (Whitelock et al. 2004). The X-ray decline starts just after phase 0.98 (or -0.02); In the 2003 minimum, there was an X-ray flare at phase 0.99 (Corcoran 2005). The minimum starts just before phase zero, and ends at phase ~ 0.03 (or ~ 1.03). The sharp decline in the IR and HeII λ 4686Å line starts at phase ~ 0 .

(3) *No hardening during the minimum.* For ~ 40 days into the minimum, the RXTE-observed 2 – 10 keV X-ray luminosity is $\sim 3 \times 10^{33}$ erg s $^{-1}$ (for a distance of 2.3 kpc to η Car), with large relative variations, e.g., spikes (Corcoran 2005). However, the RXTE field of view includes both the central source and the surrounding nebula. The X-ray emission by the extended nebula is much softer than emission from the stellar source (Hamaguchi et al. 2005), hence RXTE finds a softer spectrum during the minimum (Corcoran 2005), which is not intrinsic to the central source. Hamaguchi et al. (2005) observed η Car 24 days into the minimum (on 2003-07-22) with *XMM-Newton*. Despite the huge decline, the X-ray spectrum does not become harder. This shows that absorption cannot be the main reason for the X-ray decline. After another several days the X-ray luminosity starts to increase for a while (Corcoran 2005), and becomes harder (Corcoran 2005; Hamaguchi et al. 2005). This again contradicts an absorption effect in which a rise in flux (less absorption) would be accompanied by softening. We note that the softening in the RXTE plot of Corcoran (2005) starts a little after the decline starts. If the hardness variation was only due to the central source diminishing while the surroundings remain constant, then the total radiation observed by RXTE should have become softer at the same time the decline started. This shows that although absorption is not the main factor during the minimum, it may still play a role during the decline to, and the rise out of, the minimum. About 30 days into

the X-ray minimum, RXTE detected an increase in X-ray flux to $\sim 6 \times 10^{33}$ erg s $^{-1}$. The spectrum becomes even a little harder (Corcoran 2005). This is followed by a slow decline back to $\sim 4 \times 10^{33}$ erg s $^{-1}$ and by softening of the emission, before the steep rise out of the minimum.

(4) *Flares.* Flares occur during most of the orbit. Their effect in the RXTE 2 – 10 keV band is a $\sim 10\%$ increase in luminosity. This may indicate stochastic variations in one or two of the wind parameters (velocity; density; inhomogeneity), and/or instabilities in the wind interaction region. The flare amplitudes increase somewhat with the X-ray average luminosity after phase ~ 0.6 (Corcoran 2005). However, during the maximum period before decline, there are very strong variations, with “flares” which increase the intensity by up to $\sim 50\%$ (Corcoran 2005). Such strong flares most likely indicate much stronger instabilities in the winds interaction process. Such instabilities may lead to the formation of dense blobs in the post-shock primary wind region, which eventually are favorable for accretion by the secondary (Soker 2005b).

(5) *Cycle-to-cycle variation.* Two minima were observed in X-rays by RXTE. The X-ray luminosity at the maximum emission just prior to the X-ray minimum in 2003.5 is larger than that in 1997.9 (Corcoran 2005). The qualitative behavior is similar in the two minima, however, with similar time scales.

2.2. Proposed Model

In order for absorption to account for the deep X-ray minimum, Corcoran et al. (2001a) were required to assume that the mass loss rate from the primary in η Car increases by a factor of ~ 20 for 80 days following periastron. This model also requires the secondary to be behind the primary during periastron (Corcoran et al. 2004b). Ishibashi (2001) first showed that a semi-major axis orientation perpendicular to our line of sight provided the best fit to the asymmetry in the X-ray light curve before and after the event, if the secondary is behind the primary after the event. We note that in a recent paper Smith et al. (2004) argue that the semi-major axis of the η Car binary system is indeed more or less perpendicular to the line of sight, but the companion is not behind the primary near or after periastron, but rather the secondary is behind the primary before periastron passage. Falceta-Goncalves et al. (2005) and Abraham et al. (2005) build a different model, where the secondary is in-front of the primary during periastron; this model requires that we observe the η Car system in the orbital plane. However, from the structure of the Homunculus we believe the orbital plane is tilted by $\sim 48^\circ$ from an edge-on view (an inclination angle of $i = 42^\circ$; Smith 2002). It appears that the model of Falceta-Goncalves et al. (2005) can not work for

an inclined system, although they do not give enough details for a conclusive assessment.

In the presently proposed model, the collapse of the wind collision region onto the secondary is the reason for the sharp decline in the X-ray intensity. Figure 1 shows the proposed orbit in the top panel and the stagnation point region in the lower panel. Most of the 2 – 10 keV X-ray emission outside the X-ray minimum comes from the shocked secondary wind (e.g., Pittard & Corcoran 2002). When the two stars approach periastron, the ratio of the accretion radius of the secondary R_{acc2} , to the distance of the secondary from the stagnation point D_{g2} , increases substantially, reaching a value of ~ 0.1 , 40 days before periastron passage, and ~ 0.4 at periastron. At the same time the free fall time of cold post-shock primary wind mass elements becomes shorter, and it is no longer much larger than the flow time out of the stagnation region. As pointed out by Soker (2005b), the evolution of these two ratios strongly suggests that the stagnation point region collapses onto the secondary $\sim 0 - 40$ days before periastron passage, and the secondary starts to accrete the primary wind. This process is assumed to prevent the secondary from accelerating its wind, hence shutting-down the main source of X-ray emission, causing the minimum. The gradual collapse of the winds is associated with a rise in density and column density, which is responsible for the temporary hardening of the X-ray spectrum before minimum (Corcoran 2005).

As distance increases after periastron passage the accretion rate decreases, allowing the acceleration zone of the secondary wind to build up again $\sim 60 - 70$ days after periastron passage. As a result the wind reappears and so does the X-ray emission. Right after the minimum, the binary separation is still small and X-rays are emitted from deep in the primary wind, again through a relatively high column density, which again results in a (temporarily) hard spectrum. The progressive hardening and softening of the X-ray spectrum just outside the deep minimum is consistent with an absorption effect. Later on, as the secondary emerges from periastron, the radiation becomes softer returning to its normal orbital spectrum.

At ~ 30 days into the minimum the X-ray radiation becomes harder for ~ 25 days. This is accompanied by an increase in X-ray luminosity; this is observed in both the 1997.9 and the 2003.5 minima (Corcoran 2005). The small rise in X-ray luminosity ~ 30 days into the minimum, might be explained with our model in the following, somewhat speculative, way. For a short time during the accretion phase the specific angular momentum of the accreted mass rises, such that the accretion onto the secondary is concentrated in the equatorial plane, and part of the accreted mass is blown along the polar directions. This moderate-velocity polar outflow runs into the ambient primary wind and is subsequently shocked, which results in weak extra X-ray emission during the minimum.

Based on the results of Soker (2005b) and observations, we consider the X-ray minimum

to start $\sim 0 - 30$ days (phase -0.015 to 0) before periastron passage. In the present paper we take the accretion to start 20 days before periastron (orbital-phase -0.01), and to end 60 days after periastron, (orbital-phase 0.03). The X-ray minimum itself starts a little after accretion starts, and lasts several days less than the assumed 80 day accretion period. Any starting phase of the X-ray minimum in the range $\sim -0.04 - 0$ is acceptable in our model.

3. COLLIDING WINDS

3.1. Structure of the Flow

3.1.1. Binary orbit

The binary system parameters are as in the first paper in this series (Soker 2005b). The stellar masses are $M_1 = 120M_\odot$, $M_2 = 30M_\odot$, the eccentricity is $e = 0.9$, and orbital period 2024 days, hence the semi-major axis is $a = 16.64$ AU and periastron occurs at $r = 1.66$ AU. The mass loss rates are $\dot{M}_1 = 3 \times 10^{-4}M_\odot \text{ yr}^{-1}$ and $\dot{M}_2 = 10^{-5}M_\odot \text{ yr}^{-1}$. Ishibashi (2001) proposed that $M_2 \simeq 40M_\odot$. A more massive secondary implies even more gravity by the secondary, favoring accretion near periastron passage even further. According to Smith et al. (2003) the total primary mass loss rate is higher than $3 \times 10^{-4}M_\odot \text{ yr}^{-1}$, but with a higher mass loss rate in the polar directions and lower mass loss rate toward the equatorial plane. Since most of the X-ray emission comes from regions near the equatorial plane, we take the mass loss rate as quoted above. The primary wind velocity profile is:

$$v_1 = 500[1 - (0.4 \text{ AU}/r_1)] \text{ km s}^{-1} \quad (1)$$

where r_1 is the distance from the center of the primary. The secondary wind speed is taken to be $v_2 = 3000 \text{ km s}^{-1}$. The orbital separation r , the relative orbital velocity of the two stars v_{orb} , and the angle θ of the position of the secondary relative to the semi-major axis during periastron (see Figure 1) are plotted in the first row of Figure 2.

In the second row, the thick line represents the typical time τ_{f2} for the shocked secondary wind to flow out of the shocked region (winds interaction zone), while the thin line depicts the radiative cooling time of the shocked secondary wind $\tau_{\text{cool}2}$. In the third row of Figure 2, the distance of the stagnation point from the secondary, D_{g2} , and the Bondi-Hoyle accretion radius of the primary wind by the secondary star $R_{\text{acc}2}$, are drawn. In the fourth row the velocity of the primary wind relative to the stagnation point $v_{\text{wind}1}$ is depicted by the thick line, while the thin line represents the ratio of $\tau_{f2}/\tau_{\text{cool}2}$. For more detail on these quantities see Soker (2005b).

3.1.2. Colliding wind geometry

The colliding wind region is schematically drawn in Figure 3. The winds from the two stars produce two respective shock waves. The shocked gas flows away from the stagnation point along the contact discontinuity—the surface where the two momentum fluxes exactly balance each other and which separates the two post-shock flows. The gas is heated by the shock waves to temperatures of $\sim 10^7 - 10^8$ K and generates X-ray emission. The distances D_1 and D_2 from the binary components to the stagnation point are calculated from the equation

$$\rho_1 v_{\text{wind1}}^2 = \rho_2 v_2^2. \quad (2)$$

Here ρ_1 and ρ_2 are the pre-shock densities of the two winds, v_{wind1} is the pre-shock speed of the primary wind relative to the stagnation point (assumed to move with the secondary), and v_2 is the pre-shock speed of the secondary wind. All quantities are calculated at the stagnation point. Using equation (2) and the relation $D_1 + D_2 = r$ where r is the distance between the stars, the distance D_1 and D_2 can be found. When the effect of the gravity of the companion is included, the newly calculated distance of the stagnation point to the secondary, D_{g2} , decreases slightly. At periastron $D_{g2} \simeq 0.8D_2$.

The asymptotic half opening angle ϕ_a of the contact discontinuity, which is defined in Figure 3, is (e.g., Eichler & Usov, 1993)

$$\phi_a \sim 2.1 \left(1 - \frac{\beta^{4/5}}{4} \right) \beta^{2/3} \simeq 1 \simeq 60^\circ, \quad (3)$$

where

$$\beta \equiv \left(\frac{\dot{M}_2 v_2}{\dot{M}_1 v_1} \right)^{1/2}. \quad (4)$$

For the parameters used here $\beta \simeq 0.4$.

3.2. X-ray Emission

Usov (1992) gives an expression for the X-ray luminosity L_x later used by Ishibashi et al. (1999). However, this expression cannot be applicable here, because if we substitute the velocities and mass loss rates typical of η Car at an orbital separation of $r < 4$ AU the total X-ray emission is more than the total kinetic power of the secondary wind. This is indeed a problem in the model of Falceta-Goncalves et al. (2005). We therefore need to derive a different expression for the X-ray luminosity. The expected increase in the intrinsic luminosity with orbital separation is $1/r$ (Usov 1992), much more than that observed. The

more moderate increase of L_x with decreasing orbital separation was attributed by Ishibashi et al. (1999) and Corcoran et al. (2001) to an increase in absorption accompanying the increase in X-ray intrinsic luminosity with decreasing radius. We will assume the same.

Usov (1992) uses a cooling function $\Lambda \propto T^{1/2}$ that is appropriate for hot gas at $T \gtrsim 2 \times 10^7$ K. Since the shocked primary wind of η Car is much cooler, we need to use a more appropriate cooling function. We define $F_{AB}(T_s)$ to be the fraction of the X-ray flux emitted by the gas shocked to the temperature T_s in the range $A - B$ (in keV), out of the total flux emitted between 0.01–100 keV. The X-ray luminosity between 2 – 10 keV depends strongly on T_s . Using the APEC plasma database (Smith et al. 2001), we have calculated $F_{AB}(T_s)$ for a range of temperatures corresponding to pre-shock wind velocities (relative to the shock) of $500 \lesssim v \lesssim 2000$ km s⁻¹. We then fitted $F_{AB}(T_s)$ with a parametric form of the bremsstrahlung emissivity function to obtain:

$$F_{210} = 0.65 \exp(-2.325 \times 10^7/T_s) = 0.65 \exp\left[-6.6 \left(\frac{v}{500 \text{ km s}^{-1}}\right)^{-2}\right]. \quad (5)$$

3.2.1. Primary wind

Close to the X-ray minimum, which occurs near periastron passage, the shocked primary wind is very dense and its cooling time is much shorter than the flow time (e.g., Pittard & Corcoran 2002; Soker 2003). Therefore, we assume that any post-shock primary wind material cools instantaneously by emitting all of its thermal energy in the form of radiation. The emitted spectrum is taken to be that of gas at the post-shock temperature at the stagnation point. Since the shock front is oblique, the shock velocity and the temperature away from the stagnation point, in reality, are lower. Moreover, as the shocked primary wind loses energy, its temperature decreases. Consequently, on average, the spectrum is typical of temperatures lower than the immediate post-shock temperature. For temperatures typical of the shocked primary wind, a small decrease in the emitting gas temperature substantially reduces its contribution in the band above 2 keV. Therefore, it should be clear that our treatment overestimates the contribution of the primary wind to the X-ray emission in the 2 – 10 keV band.

From the shape of the shock wave for our relevant parameters (section 3.1) we estimate that the primary’s wind segments with $\phi \lesssim 40^\circ$ pass through a strong enough shock and heat to high enough temperature to contribute to the X-ray emission in the 2 – 10 keV band (see Fig. 3). This implies that the rate of mass entering the strong shock region is $k_1 \dot{M}_1 = (1 - \cos 40^\circ) \dot{M}_1 / 2 = 0.1 \dot{M}_1$. The pre-shock velocity of this mass is about equal to the relative velocity of the primary wind to the stagnation point, v_{wind1} , and it is plotted

in the fourth row of Figure 2. The calculation of v_{wind1} includes the wind velocity relative to the primary and the relative orbital velocity between the two stars. The acceleration of the primary wind is included by taking a lower value of v_1 close to the primary star, which increases with distance from the primary up to a terminal velocity at large distances of $v_1 = 500 \text{ km s}^{-1}$ (see Soker 2005b for more details).

The relevant velocity for the primary wind at the stagnation point is $v_{\text{wind1}} \simeq 500 \text{ km s}^{-1}$ (see fourth row of Fig. 2). For a pre-shock velocity of $v_{\text{wind1}} = 400, 500$ and 600 km s^{-1} , corresponding to post-shock temperatures of $T_{s1} = 2.2 \times 10^6, 3.5 \times 10^6$ K, and 5×10^6 K, we find $F_{210} = 2.1 \times 10^{-4}, 1.1 \times 10^{-3}$, and 5.5×10^{-3} , respectively. In other words, only a small fraction of the energy is emitted in the X-ray band. The contribution of the primary wind is, therefore:

$$L_{x1} \simeq 2.4 \times 10^{33} \left(\frac{k_1}{0.1} \right) \left(\frac{F_{210}}{0.001} \right) \left(\frac{\dot{M}_1}{3 \times 10^{-4} M_\odot \text{ yr}^{-1}} \right) \left(\frac{v_{\text{wind1}}}{500 \text{ km s}^{-1}} \right)^2 \text{ erg s}^{-1}. \quad (6)$$

The X-ray luminosity L_{x1} as a function of orbital phase is plotted as a thin solid line in the upper row of Fig. 4. The dotted line in the same figure shows the X-ray flux in the entire $0.01 - 10 \text{ keV}$, namely taking $F_{210} = 1$ in equation (6) (note the different scaling there). Considering photoelectric absorption (mostly at $2-3 \text{ keV}$), the observed luminosity reduces to $L_{x1} \lesssim 10^{33} \text{ erg s}^{-1}$ during most of the orbit, with possible intrinsic contribution of up to $L_{x1} \sim 10^{34} \text{ erg s}^{-1}$ as the system approaches periastron where v_{wind1} is high (Fig. 2). On the other hand, close to periastron, X-ray absorption is at its peak. The most important point, however, is that the primary wind is very slow, therefore the post-shock temperature is low and most of the X-ray emission is soft with negligible contribution above $\sim 3 \text{ keV}$ (Pittard & Corcoran 2002). Furthermore, the X-ray emission below 3 keV is more strongly absorbed, and one must conclude that during most of the orbit the major fraction of the observed $2 - 10 \text{ keV}$ X-ray emission comes from the secondary wind. (We emphasize again: the primary wind does emit in the $2 - 3 \text{ keV}$ band, as seen in the upper row of Figure 4, however absorption in this band is high and most of this flux never reaches the observer. In addition, for reasons stated at the beginning of this subsection, the treatment here overestimates the contribution of the shocked primary wind to the $2 - 10 \text{ keV}$ band.)

3.2.2. Secondary wind

The secondary wind is much faster ($\sim 3000 \text{ km s}^{-1}$) than the primary wind and the relevant temperature range is therefore $\sim 0.5 - 1.3 \times 10^8 \text{ K}$ for which we find an average value of $F_{210} = 0.46$. At the high temperatures and low densities typical of the secondary

wind, and in contrast with the primary wind, the radiative cooling time of the post-shock secondary wind material $\tau_{\text{cool}2}$, is much *longer* than the flow time out of the wind-collision region. This implies that the shocked secondary wind region is large, because the shock front is at a large distance from the contact discontinuity, e.g., as Pittard et al. (2002) simulate for the massive binary system WR 147. This is schematically drawn in Fig. 3.

For the purpose of studying the X-ray minimum, it is adequate to take the contribution of the secondary wind to the X-ray luminosity as follows. We assume that about half of the mass blown by the secondary star is shocked in a shock front perpendicular to the wind velocity. We then assume that the X-ray luminosity is determined by how much of the thermal energy of the shocked gas is radiatively emitted as X-rays before the gas cools adiabatically. The radiative emission lasts for time scales of the order of the radiative cooling time $\tau_{\text{cool}2}$, while adiabatic cooling takes place on the flow time scale τ_{f2} . Therefore, the total X-ray energy emitted is a fraction $k_2\tau_{f2}/\tau_{\text{cool}2}$ of the thermal energy of the post-shock gas. Here $\tau_{f2} \equiv D_{g2}/v_2$ is the characteristic flow time of the shocked wind out of the interaction region, where D_{g2} is the distance of the stagnation point from the secondary. The value of $\tau_{f2}/\tau_{\text{cool}2}$ is plotted in the last row of Fig. 2. The contribution of the shocked secondary wind material to the X-ray luminosity in the energy range $A - B$ can therefore be written as:

$$L_{x2} = \frac{1}{4} \dot{M}_2 v_2^2 F_{AB}(T_s) \frac{\tau_{f2}}{\tau_{\text{cool}2}} k_2. \quad (7)$$

Substituting typical values in equation (7) gives for the 2–10 keV range:

$$L_{x2} = 6.5 \times 10^{34} \left(\frac{F_{210}}{0.46} \right) \left(\frac{\dot{M}_2}{10^{-5} M_\odot \text{ yr}^{-1}} \right) \left(\frac{v_2}{3000 \text{ km s}^{-1}} \right)^2 \left(\frac{\tau_{f2}/\tau_{\text{cool}2}}{0.01} \right) k_2 \text{ erg s}^{-1}. \quad (8)$$

As shown by Pittard & Corcoran (2002), Kelvin-Helmholtz instability modes develop on the contact discontinuity. This instability indirectly enhances the X-ray emission by two effects: (i) the large "tongues" slow-down the velocity of the shocked secondary wind, increasing the effective outflow time of shocked secondary wind near the contact discontinuity; and (ii) the Kelvin-Helmholtz instability mixes hot, shocked secondary-wind gas with cool, dense shocked primary-wind gas. This mixing causes a small fraction of the shocked secondary wind to cool to low temperatures releasing most of its energy (and not just a fraction of $\tau_{f2}/\tau_{\text{cool}2}$). These effects, as well as our ignorance of the exact values of the secondary wind speed and mass loss rate, are incorporated in the parameter $k_2 > 1$ which we fit to match the observed X-ray luminosity. The luminosity L_{x2} according to equation (8) with

$k_2 = 2$ is plotted as the thick line in the upper row of Figure 4 where it can be seen to dominate L_{x1} .

3.3. X-ray Absorption

If the X-rays from η Car are observed through the primary wind, absorption is inevitable, but its magnitude depends on the wind parameters, flow parameters, and system orientation. Firstly, the soft (2 – 5 keV) and hard (7 – 10 keV) bands are generally emitted from different regions. The hard X-rays come mainly from regions closer to the stagnation point, where the shock wave is strong and post-shock temperature is $\sim 10^8$ K. This region is marked by capital bold-face letters ‘X’ in Figure 6. Away from the stagnation point, the gas cools adiabatically and the X-rays become softer. Thus, we expect the column density toward the hard X-ray regions to be somewhat higher than that toward the soft X-ray region. Although the soft X-ray regions are less obscured, absorption of soft X-rays is high enough to explain the X-ray hardening effect just prior and just after the X-ray minimum. As our main goal is to explain the X-ray light curve, including the minimum, in the present work we will not model the 2 – 5 keV and 7 – 10 keV bands separately, but treat the entire 2–10 keV band together.

Secondly, for some orientations and some of the time, the X-ray emission could be observed through the tenuous secondary wind instead of through the bulk of the dense primary wind, which would imply a lower column density. These orientations are represented in Fig. 6 by the narrow arrows. For observer A in Fig. 6, this occurs after the X-ray minimum, while for observer B this occurs before the X-ray minimum. The winds collision model implies significant absorption of the X-ray emission during the X-ray maximum just before the X-ray minimum. This rules out the orientation of observer B in Fig. 6. (We note that Falceta-Goncalves et al. (2005) and Abraham et al. (2005) argue to the contrary; however, they require the line of sight to be through the orbital plane, which is in contradiction with the structure of the Homunculus from which the orbital plane is deduced to be tilted by $\sim 48^\circ$ from an edge-on view (Smith 2002).) At other phases, the X-ray emission is partially absorbed by the much higher column density of the primary wind (wide arrows in Figure 6). To estimate the importance of the geometry, we assume that our line of sight is at $\sim 45^\circ$ to the orbital plane (Smith 2002). Let ϕ_a be the asymptotic half opening angle of the contact discontinuity (Fig. 3). At an angle of 45° , the projection of the half opening angle on the orbital plane, ϕ_{45} , is given by $\tan \phi_{45} = (\tan^2 \phi_a - 1)^{1/2}$. For $\phi_a = 45^\circ, 60^\circ$, and 70° , we find $\phi_{45} = 0, 54.7^\circ$ and 68.7° , respectively. Namely, if $\phi_a \leq 45^\circ$ we will always observe the X-ray emitting gas through the primary wind. For the typical parameters used

here $\phi_a \simeq 60^\circ$. Hence, $\phi_{45} \simeq 55^\circ$. Therefore, during a substantial fraction of the orbital orbit we might be observing the X-ray emission through the fast secondary wind (i.e., low column density). We do not elaborate on this effect in the present paper, because there are too many unconstrained parameters to consider: (1) There is no consensus yet on the orbital orientation (e.g., Ishibashi 2001; Smith et al. 2004). (2) The non-spherical mass loss geometry from the primary, with denser material in the polar direction (Smith et al. 2003). (3) The cone depicted in Fig. 6 actually has a spiral structure due to the orbital motion. Namely, the winds interaction region is winding around the binary system as it flows outward, like the dust in the interacting winds binary system WR 98a (Monnier et al. 1999). This includes the cool, dense post-shocked primary wind material. Hence, some absorption is expected. Each one of these three effects introduces at least one free parameter. At this stage of the development of the model, there is no point in exploring this immense parameter space. Instead, we notice that most of the absorption occurs by the primary wind in regions close to the stagnation point, and use this to build a simple geometry which includes the main features of the primary wind near the stagnation point. For comparison, we also consider the absorption for the orbital orientation proposed by Smith et al. (2004).

Following the discussion of the previous paragraph, in the present calculations we take, as our basic geometrical structure, the momentary column density through the primary wind to be that to the stagnation point, along a line of sight perpendicular to the line connecting the two stars. Taking y to be the coordinate perpendicular to the line connecting the two stars, and using $\dot{M}_1 = n\mu m_H 4\pi r_1^2 v_1$, where $r_1^2 = D_1^2 + y^2$, this hydrogen column number density can be expressed as:

$$N_{H1} = 0.43k_g \int_0^\infty \frac{\dot{M}_1}{4\pi(D_1^2 + y^2)v_1\mu m_H} dy, \quad (9)$$

where μm_H is the mean mass per particle in a fully ionized gas, n is the total number density, 43% of which are hydrogen nuclei, and k_g is a factor that depends on the geometry and orientation. It is used here to compensate for the many unknown parameters. Performing the integral under the assumption of constant v_1 , and substituting typical values near periastron gives

$$N_{H1} = 1.3 \times 10^{24} \frac{\dot{M}_1}{3 \times 10^{-4} M_\odot \text{ yr}^{-1}} \left(\frac{v_1}{500 \text{ km s}^{-1}} \right)^{-1} \left(\frac{D_1}{1 \text{ AU}} \right)^{-1} k_g \text{ cm}^{-2}. \quad (10)$$

At apastron the binary separation is 31.6 AU, and the stagnation point is a distance $D_1 = r - D_{g2} \simeq 22$ AU from the primary, which from Eq. 10 yields a column density at apastron of $N_{H1p} \simeq 6 \times 10^{22} \text{ cm}^{-2}$. Observations indicate a column density of $N_H \simeq 3 \times 10^{22} \text{ cm}^{-2}$ during most of the orbit (Ishibashi et al. 1999; Corcoran et al. 2001). We therefore take

$k_g = 0.5$ in the present work, although this value can be larger when the system emerges from the X-ray minimum.

In the second row of Fig. 4, we plot the calculated X-ray transmission factor using the column density given by equation (10) with $k_g = 0.5$. We plot the transmission separately for the soft 2–5 keV, hard 7–10 keV, and the entire 2–10 keV bands. In the third row of Fig. 4, we plot the X-ray luminosity (first row), but now including absorption. It can be seen that after absorption L_{x2} is even more dominant over L_{x1} .

The geometry used to calculate the column density in equations (9, 10) was the simplest one, and we chose it because of the many uncertainties. We could use another geometry, such as that suggested by Smith et al. (2004): The inclination angle i of our line of sight to a norm to the orbital plane is 42° , and the secondary is on the far side of the primary before reaching periastron (the semi-major axis is perpendicular to our line of sight). In this geometry, the line of sight to the stagnation point practically always goes through the primary wind, unlike some orientations shown in Fig. 6, which was plotted for the $i = 90^\circ$ case. The reason is that after periastron passage the bow shock of the secondary wind is fully recovered only at phase ~ 0.04 (see fig. 9), when the orbital angle is $\theta \sim 140^\circ$ (upper row of Figure 2). It can be shown that when the semi-major axis is perpendicular to the line of sight then the column density of the primary wind as a function of the binary azimuthal angle θ and inclination angle i is:

$$N_{H1i}(i) = \frac{0.43k_g\dot{M}_1}{4\pi\mu m_H v_1 D_1} \frac{(1 + \tan^2 i)^{1/2}}{(1 + \cos^2 \theta \tan^2 i)^{1/2}} \left[1 - \frac{2}{\pi} \tan^{-1} \frac{\sin \theta \tan i}{(1 + \cos^2 \theta \tan^2 i)^{1/2}} \right] \quad (11)$$

where θ here is negative before periastron, zero at periastron, and positive after periastron (see Fig. 1). The ratio $N_{H1i}(i = 42^\circ)/N_{H1}$ as a function of the orbital phase is plotted in the upper row of Fig. 5 for a fixed value of k_g . In the second row of Fig. 5, the absorbed X-ray luminosity is plotted with $k_g = 0.5$, but with the column density given by equation (11). The last row of Figure 5 shows the ratio of this X-ray luminosity to that shown in Fig. 4 for the $i = 90^\circ$ case. It can be seen that the only significant difference arises near periastron, where according to the proposed model, the secondary wind does not exist. We conclude that the difference between the two geometries is practically small and that the X-ray luminosity is not very sensitive to the inclination angle i (as long as i is not too small). The emission of the shocked primary wind is reduced substantially; but in our model most X-ray emission in the 2 – 10 keV bend is attributed to the shocked secondary wind anyway. To summarize, although the binary orientation assumed in calculating the absorbing column density used in equation (9) (or 10) is not the exact orientation of the binary system in η Car, it is adequate for the main goal of the present paper as it emphasizes the weak dependence of the results on the exact geometry. The orientation used in deriving equation (9) has the advantage

that it does not depend on the orientation of the periastron (ω) with respect to our line of sight. The small difference between the results obtained for the two geometries used here demonstrates that our model is neither sensitive to the orientation of the periastron nor to the inclination of the orbital plane (as long as i is not too small).

The X-ray minimum lasts ~ 70 days, the time from the beginning of the decline to the end of the rise from the minimum is ~ 120 days. According to our proposed model, the decline starts ~ 40 day before periastron passage ($r \simeq 5.3$ AU), when the absorbing column density increases and blobs from the post-shock primary wind start to be accreted. Bondi-Hoyle type accretion starts ~ 20 days before periastron ($r \simeq 3.3$ AU). The minimum starts ~ 10 days before periastron, and ends ~ 60 days after periastron ($r \simeq 7.2$ AU), taking another ~ 20 days to fully rise back ($r \simeq 8.7$ AU, and $D_1 \simeq 6$ AU). At the beginning of the decline (40 days before periastron), where the absorption effect is most significant, the column density is $N_{H1} \simeq 1.5 \times 10^{23} \text{ cm}^{-2}$ (with $k_g = 0.5$). At this column density, 29%, 83%, and 71% of the flux is transmitted through the primary wind in the 2 – 5 keV, 7 – 10 keV, and 2–10 keV bands, respectively. The rest is absorbed by the primary wind.

4. ACCRETION PHASE

4.1. Flow Structure

In the presently proposed model, the X-ray minimum is assumed to occur as the secondary accretes mass from the primary wind (Soker 2005b). The accreted mass is assumed to prevent the secondary from blowing its fast wind, thus the dominant X-ray source is turned off. The accretion flow is of the Bondi-Hoyle type (Figure 7). The very high Mach number creates an accretion shock. Because the cooling time of the post-shocked primary wind material is very short near periastron, about one percent of the flow time, (e.g., Pittard & Corcoran 2002; Soker 2003), the accretion flow can be treated as isothermal. Such a flow was simulated, e.g., by Ruffert (1996). In the following, we distinguish between segments of the primary wind impacting the secondary directly and segments that go around the secondary toward the accretion column (behind the secondary) along a curved trajectory. The basic flow structure is as follows.

The accretion column—the elongated region behind the secondary enclosed by the shocked accreted matter—is narrow (see Fig. 7) and the Mach number of the pre-shock primary wind is high. As an approximation, we take the velocity of the primary wind just before it hits the shock wave as the velocity it would have reached on the accretion line—the

Table 1: Glossary

Symbol	Meaning	Typical value
r	Binary separation	1.66 – 31.6 AU
θ	Binary azimuthal angle (Fig. 1)	$0 - 2\pi$
D_1	Distance of stagnation point from primary $D_1 = r - D_{g2}$	$\sim 0.75 r$
D_2	Distance of stagnation point from secondary; gravity neglected	$\sim 0.3 r$
D_{g2}	Distance of stagnation point from secondary; M_2 gravity included	$\sim 0.25 r$
M_1	Mass of primary	$120M_\odot$
M_2	Mass of secondary	$30M_\odot$
\dot{M}_1	Mass loss rate by primary	$3 \times 10^{-4}M_\odot \text{ yr}^{-1}$
\dot{M}_2	Mass loss rate by secondary	$10^{-5}M_\odot \text{ yr}^{-1}$
$\dot{M}_{\text{acc}2}$	Mass accretion rate of primary wind by secondary	[eq. 15] _a
v_1	Velocity of primary wind (relative to primary)	500 km s^{-1}
v_2	Velocity of secondary wind (relative to secondary)	3000 km s^{-1}
$v_{\text{wind}1}$	Velocity of primary wind relative to secondary	$\sim 500 \text{ km s}^{-1}$
R_2	Stellar radius of secondary	$\sim 0.1 \text{ AU}$
$R_{\text{acc}2}$	Accretion radius of secondary	$\sim 0.2 - 0.4 \text{ AU}$
$\tau_{\text{cool}2}$	Radiative cooling time of post shock secondary wind	[5 days] _p
τ_{f2}	Flow time of post shock secondary wind	[0.2 days] _p
F_{210}	Fraction of the X-ray energy emitted in the 2 – 10 keV band	0-1
L_{x1}	Unabsorbed X-ray luminosity of the shocked primary wind	eq. (6)
L_{x2}	Unabsorbed X-ray luminosity of the shocked secondary wind	eq. (7)
L_{xa1}	Unabsorbed X-ray luminosity of accreted primary wind	[eq. (18)] _a
L_{xa2}	Unabsorbed X-ray luminosity of primary wind hitting the secondary	[eq. (19)] _a
N_{H1}	Hydrogen column density of obscuring primary wind	$\sim 10^{23} \text{ cm}^{-2}$
k_1	Fraction of primary wind that is strongly shocked	~ 0.1
k_2	Parameter adjusting the X-ray luminosity of secondary wind	~ 2
k_g	Parameter adjusting column density of obscuring primary wind	$\sim 0.5 - 1$
i	Inclination angle (of line of sight to the norm of the orbital plane)	$0 - \pi/2$
v_{c1}	Pre-shock velocity of the primary wind on the accretion line	[eq. 13] _a
v_{ct1}	Tangential component of v_{c1}	[eq. 14] _a
$d\dot{m}/dz$	Rate of mass hitting the accretion column per unit length	[eq. 16] _a
z	Distance from secondary on the accretion line (Fig. 7)	
z_{min}	Minimum distance of accretion shock from secondary	[0.1 AU] _a

Notes: []_p indicates values given at periastron.

[]_a indicates values defined only for the ~ 80 days accretion period.

symmetry line behind the accreting body. Using the definition of $R_{\text{acc}2}$

$$R_{\text{acc}2} = \frac{2GM_2}{v_{\text{wind}1}^2} = 0.2 \left(\frac{M_2}{30M_\odot} \right) \left(\frac{v_{\text{wind}1}}{500 \text{ km s}^{-1}} \right)^{-2} \text{ AU}, \quad (12)$$

this velocity can be found from energy conservation to be:

$$v_{c1} = v_{\text{wind}1} \left(1 + \frac{R_{\text{acc}2}}{z} \right)^{1/2} \quad (13)$$

where z is the distance from the secondary along the accretion line. The component in the perpendicular direction with respect to the accretion line of the primary-wind velocity before hitting the accretion-column shock $v_{ct1}(z)$, is found from angular momentum conservation. Assuming the stream lines of the primary wind to be parallel at large distances from the secondary, we can write

$$v_{ct1} = v_{\text{wind}1} \left(\frac{R_{\text{acc}2}}{z} \right)^{1/2}. \quad (14)$$

Simulations of high Mach number, nearly-isothermal flows (e.g., Ruffert 1996) show that the flow structure is very similar to that of the classical Bondi & Hoyle (1944) accretion flow. The total accreted mass can be approximated for our purposes as follows:

$$\dot{M}_{\text{acc}2} \simeq \pi \rho_0 R_{\text{acc}2}^2 v_0 = 0.01 \dot{M}_1 \left(\frac{r}{1 \text{ AU}} \right)^{-2} \left(\frac{R_{\text{acc}2}}{0.2 \text{ AU}} \right)^2 \left(\frac{v_1}{500 \text{ km s}^{-1}} \right)^{-1} \left(\frac{v_{\text{wind}1}}{500 \text{ km s}^{-1}} \right), \quad (15)$$

where we take the density far upstream to be equal to the density at the location of the secondary $\rho_0 = \rho_1(r) = \dot{M}_1/(4\pi r^2 v_1)$, and the upstream speed is $v_0 = v_{\text{wind}1}$. The mass accretion rate as function of the orbital phase is plotted in the upper panel of Figure 8, only during the orbital phases where according to our model accretion occurs. Part of the accreted mass hits the accretion line in the range $z_{\text{min}} \lesssim z \lesssim R_{\text{acc}2}$, while another fraction of the incoming mass, $\sim (z_{\text{min}}/R_{\text{acc}2})\dot{M}_{\text{acc}2}$, hits the accretion shock close to the accreting body. The rate of mass hitting the accretion column per unit length is (Bondi & Hoyle 1944)

$$\frac{d\dot{m}_z}{dz} = \pi \rho_1(r) v_{\text{wind}1} R_{\text{acc}2}. \quad (16)$$

4.2. X-ray Emission due to Accretion

The material with impact parameter $b \lesssim R_{\text{acc}2}$ will be attracted by the secondary's gravity and flow towards the accretion line, passing through the shock almost perpendicular

to the shock front. This gas is subsequently heated to a post-shock temperature appropriate for its incoming velocity, which is given by equation (13). We assume this gas to be completely thermalized. The thermal energy gained per unit length is:

$$\frac{d\dot{E}_{a1}}{dz} = \frac{1}{2} \frac{d\dot{m}_z}{dz} v_{c1}^2. \quad (17)$$

We further assume that the cooling time is very short and that all this energy is radiated away giving rise to an X-ray luminosity in the 2 – 10 keV range of:

$$L_{xa1} = \frac{1}{2} \int_{z_{\min}}^{R_{\text{acc}2}} F_{210}(z) \frac{d\dot{m}_z}{dz} v_{c1}^2 dz, \quad (18)$$

where F_{210} depends on z through the dependence of the post-shock temperature T_s on v_{c1} .

The material impacting the secondary directly is also assumed to pass through the accretion shock perpendicular to the shock front at a distance z_{\min} from the secondary, with a speed given by equation (13) with $z = z_{\min}$. We take z_{\min} to be approximately the radius of the secondary star $R_2 \simeq 22R_{\odot} \simeq 0.1$ AU (Verner et al. 2005). This contribution to the X-ray luminosity is therefore

$$L_{xa2} = \frac{1}{2} \frac{z_{\min}}{R_{\text{acc}2}} \dot{M}_{\text{acc}2} (F_{210} v_{c1}^2)_{z=z_{\min}}. \quad (19)$$

For $z_{\min} = 0.1$ AU and near periastron we find for the pre-shock speed $v_{c1} \simeq 900$ km s⁻¹, and for the post-shock temperature $T_s \simeq 10^7$ K and $F_{210} \simeq 0.08$. We scale equation (19) to find

$$L_{xa2} \simeq 4 \times 10^{34} \left(\frac{z_{\min}/R_{\text{acc}2}}{0.5} \right) \left(\frac{\dot{M}_{\text{acc}2}}{3 \times 10^{-6} M_{\odot} \text{ yr}^{-1}} \right) \left(\frac{F_{210}}{0.08} \right) \left(\frac{v_{c1}}{1000 \text{ km s}^{-1}} \right)^2 \text{ erg s}^{-1}. \quad (20)$$

The two contributions to the intrinsic luminosity in the 2 – 10 keV band are plotted in the second panel of Figure 8. The third panel shows the total luminosity of the two contributions, namely, in the 0 – ∞ keV band. This intrinsic luminosity is much larger than the luminosity observed during the minimum. However, during the minimum, the column density through the primary wind is considerable ($N_{H1} > 10^{23}$ cm⁻²) and it totally absorbs the X-ray accretion source. We find that accretion cannot even account for the weak X-ray flux during the minimum as demonstrated below.

The mass hitting the accretion column at $z \gtrsim R_{\text{acc}2}$, is not accreted by the secondary. It passes through an oblique shock at an angle of θ between the inflow direction and the shock front with $\tan \theta \simeq v_{ct1}/v_{\text{wind}1}$ (or $\sin \theta = v_{ct1}/v_{c1}$). This post-shock temperature is less than the post-shock temperature of the primary wind when accretion does not occur. Hence this

gas emits soft X-rays, which are totally absorbed by the primary wind. We do not consider its contribution in this paper.

As the primary wind flows toward the accreting body its density increases. Therefore, the column density to the X-ray emitting regions here is somewhat larger than that in equation (10). In addition, the density in the accretion column is very large making it completely opaque. Therefore, only \sim half of the intrinsic luminosity can be observed. For the emerging radiation, we take the column density of equation (10), but with $r \simeq 2$ AU replacing D_1 , and a lower value for v_1

$$N_{H1} = 10^{24} \frac{\dot{M}_1}{3 \times 10^{-4} M_\odot \text{ yr}^{-1}} \left(\frac{v_1}{400 \text{ km s}^{-1}} \right)^{-1} \left(\frac{r}{2 \text{ AU}} \right)^{-1} \text{ cm}^{-2}. \quad (21)$$

The expected X-ray emission given by equations (18) and (20), including absorption (eq. 21) is plotted in the lower panel of Figure 8. This radiation is soft, with most of the contribution to the 2 – 10 keV band coming from radiation in the 2 – 3.5 keV energy range. These simplified estimates clearly show that the soft emission due to accretion together with the high column density it needs to traverse rules out this component as a candidate for the weak X-ray emission during the minimum. A different alternative is pursued in the next subsection.

4.3. X-ray Emission during the Minimum

The main goal of the present paper is to show that the X-ray behavior up to the minimum can be explained by the assumed orbital parameters and by the variation of the radiative cooling timescale of the secondary’s wind relative to its flow timescale. The present subsection, on the other hand, is more speculative. We put forward a suggestion for the nature of the very weak X-ray emission during the minimum. We already showed that X-ray emission due to accretion cannot explain even the weak X-rays observed during the minimum. Because of the speculative nature of this subsection, the treatment is more qualitative. We suggest that the weak X-ray emission during the minimum, with its variation in hardness and intensity (see property 3 in section 2.1), could come from two different components: (*i*) an almost constant weak contribution from old shocked secondary wind, termed here the residual component; and (*ii*) a possible temporary collimated outflow resulting from accretion of mass with relatively high specific angular momentum. These two components are treated in the next two subsections.

We do not attempt to refute other contributions, e.g., other stars in the field, and more important the possibility that most of the X-ray emission during the X-ray minimum comes

from reflected light by the nebula (Hamaguchi et al. 2005); time delay ensures that the X-ray emission is observed during the minimum (Corcoran et al. 2004a). We only point out that other processes should be considered as well, before further observations and calculations will reveal the most significant process contributing to the X-ray emission and its variability during the minimum.

4.3.1. Residual emission

We propose that some fraction of the soft and weak X-ray emission observed even during the minimum results from previously shocked secondary wind segments. This residual emission exists basically along the entire orbit, but it can be noticed only after the main X-ray source has been shut down.

During the winds collision phase, the shocked secondary wind forms a hot bubble flowing away from the secondary in what we term the secondary hot-tail, winding around the binary system as it flows outward, like the dust in the interacting winds binary system WR 98a (Monnier et al. 1999). The shocked secondary wind is engulfed eventually by the slower primary wind, and expands with it to large distances at a speed of v_1 . We wish to crudely estimate the contribution of such a bubble to the X-ray emission. This crude estimate is by no means a replacement for a full 3-dimensional numerical simulation of this flow, but it does give a rough idea of its expected X-ray luminosity.

Let the main contribution to the residual emission come from gas shocked during an average time t_r before present, where t_r is a substantial fraction of the orbital period. Let a fraction q_m of the mass blown by the secondary during this time, $q_m \dot{M}_2 t_r$, be enclosed in a fraction q_V of the volume $4\pi(v_1 t_r)^3/3$. Because of the expansion, this gas is much cooler than the post strong-shock temperature of $\sim 10^8$ K. Say $T(t_r) \sim 10^7$ K, for which the contribution of the cooling gas to the emission in the 2–10 keV band is only $F_{210} \sim 0.06$ (eq. 5). Because of the expansion to large distances, this emission is hardly absorbed in comparison to the case for the accretion X-rays, although some absorption still exists. Taking gas at $\sim 10^7$ K, we find the X-ray emission to be:

$$L_{x-\text{res}} \sim 10^{34} \frac{q_m^2}{q_V} \left(\frac{F_{210}}{0.05} \right) \left(\frac{t_r}{1 \text{ yr}} \right)^{-1} \left(\frac{\dot{M}_2}{10^{-5} M_\odot \text{ yr}^{-1}} \right)^2 \left(\frac{v_1}{500 \text{ km s}^{-1}} \right)^{-3} \text{ erg s}^{-1}. \quad (22)$$

This suggests that old shocked secondary wind might in principle account for a significant fraction of the soft $\sim 3 \times 10^{33}$ erg s $^{-1}$ emission during the X-ray minimum. In a future paper the spectrum of this radiation will be compared with observation.

4.3.2. Collimated outflow during the accretion phase

We consider the specific angular momentum of the accreted matter j_a , and compare it to $j_2 = (GM_2R_2)^{1/2}$, the specific angular momentum of a particle in a Keplerian orbit at the equator of the accreting star of radius R_2 . When a compact secondary star moves in a circular orbit and accretes from the wind of a mass losing star, such that the accretion flow reaches a steady state, the ratio of the specific angular momenta is (Soker 2001)

$$1 < \frac{j_a}{j_2} \simeq 0.1 \eta \left(\frac{M_1 + M_2}{150M_\odot} \right)^{1/2} \left(\frac{M_2}{30M_\odot} \right)^{3/2} \left(\frac{R_2}{20R_\odot} \right)^{-1/2} \left(\frac{r}{2 \text{ AU}} \right)^{-3/2} \left(\frac{v_{\text{wind1}}}{400 \text{ km s}^{-1}} \right)^{-4}, \quad (23)$$

where η is the ratio of the accreted angular momentum to that entering the Bondi Hoyle accretion cylinder. There is a net accreted angular momentum because more mass is accreted by the secondary from the denser region facing the primary than from the other side, behind the secondary. When a steady state accretion flow is reached, the accretion column (and the accretion line) bends toward the lower density region, partially compensating for its lower density, and reducing the net accreted angular momentum. For this case numerical simulations show that $\eta \sim 0.2$ (e.g., Ruffert 1999). However, here no steady state is reached around phase ~ 0.004 , when the accretion radius increases by a large factor in a short time (Figure 2). This increases the mass accretion rate in a short time (Figure 8) and therefore the accretion column has no time to bend and reduce the specific angular momentum of the accreted gas. This is the reason for taking $\eta = 1$ here.

As seen, at phase ~ 0.004 , which occurs ~ 8 days after periastron, the specific angular momentum is quite large, although still less than that required to form an accretion disk ($j_a/j_2 > 1$). This implies that the accreted mass will be concentrated near the equatorial plane, with lower density regions along the polar directions. Consequently, the strong wind blown by the secondary (when undisturbed) is not efficiently suppressed along the polar directions, and together with a disk wind from the accreted matter lead to the formation of jets or a biconical collimated wind. This wind is then shocked by the impact of the ambient primary wind, and emits the low-level X-rays observed in the middle of the minimum. This emission is highly obscured by the high column density of the primary wind, hence it contributes mostly in the hard band. We show that the X-ray emission during minimum can be fitted by reasonable parameters. Let us take the polar outflow to be at a speed of $v_p = 2000 \text{ km s}^{-1}$, with the mass outflow rate being a fraction of 0.05 of the accreted mass. Taking the accretion rate at phase 0.05 (10 days after periastron passage) from our calculations (upper panel of Figure 8) to be $\sim 10^{-6}M_\odot \text{ yr}^{-1}$, the total kinetic energy in this polar outflow is $L_{\text{p-kin}} \sim 6 \times 10^{34} \text{ ergs}^{-1}$. For a column density of 10^{24} cm^{-2} , all the soft X-ray is absorbed while the hard X-rays, comprising ~ 0.4 of the flux, is reduced by a factor of ~ 5 ,

giving a luminosity of $L_{p-x} \simeq 5 \times 10^{33} \text{ ergs}^{-1}$. This hints that a short-duration collimated outflow might account for the increase in the middle of the minimum. On even shorter time scales and smaller amplitudes, stochastic variations in the accretion process—both mass accretion rate and angular momentum accretion rate—which are well documented in numerical simulations (Ruffert 1996), might lead to the small spikes observed during the minimum.

5. DISCUSSION AND SUMMARY

As was shown by Soker (2005b), the effect of the gravity of the secondary star on the primary wind becomes significant as the system approaches periastron. Cold and dense blobs are likely to form in the post-shock primary-wind region, which becomes unstable. It seems plausible that close to periastron passage, when the secondary’s gravity becomes significant, these dense blobs will be accreted by the secondary. Adopting the hypothesis of Soker (2005b), we have *assumed* that these segments of the primary wind, which are accreted, vigorously disrupt the acceleration zone of the secondary wind, so that the secondary wind ceases to exist. The formation of cold blobs will be verified in a future paper via 3D-gasdynamical numerical simulations. The effect of binary accretion on the launch of stellar winds will have to be studied theoretically in the future by examining the sensitivity of the wind acceleration zone in O stars to accreted cold gas.

In the present paper, the accretion of dense blobs is assumed to start $\sim 40 - 50$ days before periastron passage (orbital phase (~ -0.025)– $\sim (-0.02)$), and the Bondi-Hoyle type accretion flow (Fig. 7) is assumed to start ~ 20 days before periastron passage (orbital phase ~ -0.01); several days later, the (almost flat) X-ray minimum starts. As can be seen from the upper panel of Figure 8, ~ 60 days after periastron passage (orbital phase $\sim +0.03$) the accretion rate diminishes and it is *assumed* that the secondary star builds back its acceleration zone and its wind reappears. This is when the system starts to get out of the X-ray minimum, a process lasting ~ 20 days.

An interesting feature of the proposed model is the asymmetry around periastron in the relevant properties. The asymmetry results from the asymmetry of the relative velocity of the primary and secondary winds at the stagnation point. As the two stars approach each other, the relative velocity is higher than when they recede. This can be seen in the lower row of Figure 2. This effect causes the stagnation distance D_{g2} , the accretion radius R_{acc2} , the post-shock primary wind temperature, and other quantities to acquire asymmetric values about periastron passage.

In the proposed model the steep decline in the X-ray emission is due to the collapse

of the stagnation-point region onto the secondary, very close to periastron passage (Soker 2005b). The collapse starts a few weeks before periastron passage, when the secondary’s gravity at the stagnation point becomes significant. This occurs when the ratio of the accretion radius to the stagnation distance $R_{\text{acc}2}/D_{g2}$ increases to $\sim \text{few} \times 0.1$. For the assumed wind parameters in the η Car system, when this occurs, the ratio of the outflow time of the shocked primary wind, τ_{f1} , to the free fall time τ_{ff2} , becomes $\sim \text{few} \times 0.1$ as well, further supporting the importance of accretion. At present, we can not say what exact value of these ratios is needed for accretion to start. This would require 3D hydrodynamical numerical simulations. Furthermore, there are large uncertainties in the binary and wind parameters of η Car. Phenomenologically, what we can say is that the accretion model can account for the behavior around the X-ray minimum of η Car if accretion starts when $R_{\text{acc}2}/D_{g2} \simeq 0.2$ (Soker 2005b). This occurs when the stagnation point distance from the secondary is $D_{g2} \simeq 0.6$ AU. We therefore assume that accretion starts at that phase. The collapse occurs over a time period of a few times the free-fall time from the stagnation point to the secondary

$$\tau_{\text{ff}2} = 5.5 \left(\frac{M_2}{30M_{\odot}} \right)^{-1/2} \left(\frac{D_{g2}}{0.6 \text{ AU}} \right)^{3/2} \text{ day}. \quad (24)$$

The details of this process requires 3D numerical simulations, which are beyond the scope of the present paper. We therefore make do with a simple phenomenological approach. The start of the minimum is assumed to be the time when τ_{f1}/τ_{ff2} and $R_{\text{acc}2}/D_{g2}$ reach some critical value. From the X-ray lightcurve we assume the minimum starts when τ_{f1}/τ_{ff2} and $R_{\text{acc}2}/D_{g2}$ reach ~ 0.25 and ~ 0.2 , respectively. We assume that the minimum ends when these ratios fall back to these same values. Values of $\tau_{f1}/\tau_{ff2} \simeq 0.25$ and $R_{\text{acc}2}/D_{g2} \sim 0.2$ yields a duration of ~ 70 days for the minimum (Soker 2005b), in good agreement with observations. We assume a simple linear approximation for the decline to minimum and subsequent recovery. We take the significant contributions to the total X-ray luminosity L_{210} in our simple model, to be

$$L_{210}(p) = L_{x\text{-res}} + \begin{cases} L_{x1} + L_{x2} & p < -0.015 \quad \text{or} \quad p > 0.04 \\ (-0.005 - p)(L_{x1} + L_{x2})/0.01 & -0.015 \leq p < -0.005 \\ 0 & -0.005 \leq p < 0.03 \\ (p - 0.03)(L_{x1} + L_{x2})/0.01 & 0.03 \leq p \leq 0.04, \end{cases} \quad (25)$$

where the phase p is defined in the range $-0.5 \leq p < 0.5$. We have included L_{x1} and L_{x2} from equations (6) and (8), but we ignore, for the present purpose, the small contributions of accretion and the residual emission mechanisms during the minimum (sections 4.3.1 and 4.3.2). In order to compare with observations, we need to consider absorption. The absorbed X-ray luminosity, namely, L_{210} but with the absorption taken into account is given in Figure

4. The final X-ray luminosity predicted by our model is drawn in Figure 9 together with the data from Corcoran (2005).

The binary system’s parameters were chosen here from the literature on η Car, and following Soker (2005b). We note that for different parameters, the proposed accretion scenario might even be more plausible. Changing the secondary mass from $M_2 = 30M_\odot$ to $M_2 = 40M_\odot$ (Ishibashi 2001), and keeping the eccentricity and orbital period unchanged, will not affect much the periastron distance. However, the accretion radius will increase by a factor of ~ 1.3 , making accretion more likely. However, to make the ratio $R_{\text{acc}2}/D_{g2} > 0.5$ at phase ~ -0.01 (when accretion starts) will require the secondary mass to be $M_2 > 60M_\odot$, which seems unlikely.

More likely to influence this ratio is a lower primary wind speed near periastron. If the wind speed is low, say 30% of the 500 km s^{-1} assumed here near periastron, then the relative velocity of the secondary to the primary wind will basically be the orbital speed, $\sim 250 \text{ km s}^{-1}$ at phase -0.01 , instead of $\sim 500 \text{ km s}^{-1}$. The distance to the stagnation point D_{g2} will not change much, because the lower speed causes an increase in the primary wind density. The accretion radius will be ~ 4 times its value in the present case, bringing the ratio $R_{\text{acc}2}/D_{g2}$ to about unity. Moreover, the slower primary wind will increase the outflow time of the postshock gas τ_{f1} , by that increasing the ratio τ_{f1}/τ_{f2} . The slower primary wind speed may result from enhanced mass loss rate as a result of the influence of the companion, or from extended wind acceleration zone. The point is that parameters might be more favorable for the accretion scenario than those used by Soker (2005b), but not by much.

We do not try to match the observation point by point, but rather to catch the general behavior with emphasize on the X-ray minimum. We use $k_2 = 2$ to match the observation near apastron, when attenuation is weak. We then find that the luminosity before and after minimum can be matched quite well with column density as given by equation (10) with $k_g = 0.5 - 1$. In the upper row on Figure 9 we draw the expected X-ray luminosity in the 2–10 keV band according to our model for $k_g = 0.5$ (thick line) and $k_g = 1$ (thin line). In the lower row the $k_g = 0.5$ case is compared with the X-ray flux covering two spectroscopic events (two thin lines). By playing more with the several parameters, like the winds properties and eccentricity, an even better match can be obtained. Even if instead of taking the absorbing column density according to equation (10), we assume an inclination angle $i = 42^\circ$ and use equation (11) we still get a good fit. This result is illustrated by the dashed line in the lower right panel of Figure 9. In short, with the present model we already (*i*) strengthen previous results (e.g., Pittard et al. 1998; Ishibashi et al. 1999; Corcoran et al. 2001a; Pittard & Corcoran 2002) that the X-ray emission can be explained by wind collision and (*ii*) achieve

our main goal of explaining the X-ray light curve, and in particular demonstrating that the shutting down of the secondary wind might account for the X-ray minimum.

We refer now to the cycle-to-cycle variation (property 5 in section 2.1). In the winds collision model the higher maximum X-ray luminosity prior to the 2003.5 minimum compared to that prior to the 1997.9 minimum, can be accounted for by either less obscuration by the dense primary wind in the 2003.5 minimum, and/or a higher mass loss rate from the secondary in the 2003.5 minimum. For example, if the primary has the same mass loss rate in the two minima, but it is faster in that of 2003.5, then it has two effects to enhance the observed X-ray flux: (*i*) it pushes the stagnation point closer to the secondary where the secondary wind is denser, therefore radiates a higher fraction of its thermal energy; and (*ii*) the higher velocity implies lower density, thus less absorption. The data are not of high enough quality to distinguish between these two possibilities. The qualitative similarity in the two minima is expected in our model, as the binary parameters (stellar masses; eccentricity; orbital period) did not change, and the differences in winds parameters are not sufficiently large to affect the collapse of the winds interaction region.

It is not straight forward that our results of the X-ray emission are similar to that of Corcoran et al. (2001) and Ishibashi et al. (1999), because they use a formula (eq. 1 in Ishibashi et al. 1999) based on the results of Usov (1992). However, Usov (1992) derived these formulae for binary systems with weaker winds. Near periastron this equation (eq. 1 of Ishibashi et al. 1999) gives an unabsorbed X-ray luminosity greater than the total kinetic power in the two winds. This is the reason that we used a different formula (our eq. 7). We are gratified that we could account for the general behavior of the X-ray emission.

We thank an anonymous referee for very useful comments. This research was supported by the Israel Science Foundation, grant 28/03 and by the Asher Space Research Institute.

REFERENCES

- Abraham, Z., Falceta-Goncalves, D., Dominici, T. P., Caproni, A., & Jatenco-Pereira, V. 2005, MNRAS, 364, 922
- Bondi, H., & Hoyle, F. 1944, MNRAS, 104, 273
- Corcoran, M. F. 2005, AJ, 129, 2018 (digital data were taken from:
http://lheawww.gsfc.nasa.gov/users/corcoran/eta_car/etacar_rxte_lightcurve/)
- Corcoran, M. F., Hamaguchi, K., Gull, T., et al. 2004a, ApJ, 613, 381 (astro-ph/0406180)
- Corcoran, M. F., Pittard, J. M., Stevens, I. R., Henley, D. B., & Pollock, A. M. T. 2004b, in the Proceedings of "X-Ray and Radio Connections", Santa Fe, NM, 3-6 February,

- 2004 (astro-ph/0406294)
- Corcoran, M. F., Ishibashi, K., Swank, J. H., & Petre, R., 2001a, *ApJ*, 547, 1034
- Corcoran, M. F., Swank, J. H., Petre, R. et al. 2001b, *ApJ*, 562, 1031
- Damineli, A. 1996, *ApJ*, 460, L49
- Damineli, A., Conti, P. S., & Lopes, D. F. 1997, *NewA*, 2, 107
- Damineli, A., Kaufer, A., Wolf, B., Stahl, O., Lopes, D. F., & de Araujo, F. X. 2000, *ApJ*, 528, L101
- Duncan, R. A., & White, S. M. 2003, *MNRAS*, 338, 425
- Davidson, K., & Humphreys, R. M. 1997, *ARA&A*, 35, 1
- Eichler, D., Usov, V. 1993, *ApJ*, 402, 271
- Falceta-Goncalves, D., Jatenco-Pereira, V., & Abraham, Z. 2005, *MNRAS*, 357, 895
- Fernandez Lajus, E., Gamen, R., Schwartz, M., Salerno, N., Llinares, C., Farina, C., Amorin, R., & Niemela, V. 2003 *Information Bulletin on Variable Stars*, 5477, 1 (astro-ph/0311437)
- Hamaguchi, K., Corcoran, M. F., Gull, T., White, N. E., Damineli, A., & Davidson, K. 2005 (astro-ph/0411271) proceeding of the workshop "Massive Stars in Interacting Binaries"
- Jahanara, B., Mitsumoto, M., Oka, K., Matsuda, T., Hachisu, I., & Boffin, H. M. J. 2005, *A&A*, 441, 589
- Iping, R. C., Sonneborn, G., Gull, T. R., Massa, D. L., & Hillier, D. J. 2005, *ApJ*, 633, L37
- Ishibashi, K. 2001, in *ASP Conf. Ser. 242, η Carinae and Other Mysterious Stars*, ed. T. R. Gull, S. Johansson, & K. Davidson (San Francisco: ASP), 53
- Ishibashi, K., Corcoran, M. F., Davidson, K., Swank, J. H., Petre, R., Drake, S. A., Damineli, A., & White, S. 1999, *ApJ*, 524, 983
- Ishibashi, K., Gull, T., Davidson, K. et al. 2003, *AJ*, 125, 3222
- Martin, J. C., Davidson, K., Humphreys, R. M., Hillier, D. J., & Ishibashi K. 2005, *Astrophysical Journal*, (astro-ph/0504151)
- Mitsumoto, M., et al. 2005, *Astronomy Reports*, 49, 884 (astro-ph/0510175)
- Monnier, J. D., tuthill, P. G., & Danchi, W. C. 1999, 525, L97
- Pittard, J. M., & Corcoran, M. F. 2002, *A&A*, 383, 636
- Pittard, J. M., Stevens, I. R., Corcoran, M. F., & Ishibashi, K. 1998, *MNRAS*, 299, L5

- Pollock, A. M. T., Corcoran, M. F., Stevens, I. R., & Williams, P. M. 2005, *ApJ*, 629, 482
- Ruffert, M. 1999, *A&A*, 346, 861
- Ruffert, M. 1996, *A&A*, 311, 817
- Skopal, A. 2005, *A&A*, 440, 995
- Smith, R.K., Brickhouse, N.S., Liedahl, D.A., & Raymond, J.C., 2001, *ApJ*, 556, L91
- Smith, N. 2002, *MNRAS*, 337, 1252
- Smith, N., Davidson, K., Gull, T.R., Ishibashi, K., & Hillier, D.J. 2003, *ApJ*, 586, 432
- Smith, N., Morse, J. A., Collins, N. R., & Gull, T. R. 2004, *ApJ*, 610, L105 (astro-ph/0406408)
- Soker, N. 2001, *ApJ*, 558, 157
- Soker, N. 2003, *ApJ*, 597, 513
- Soker, N. 2005a, *ApJ*, 619, 1064
- Soker, N. 2005b, *ApJ*, 635, 540
- Steiner, J. E., & Daminieli, A. 2004, *ApJ*, 612, L, 133
- Usov, V. V., 1992, *ApJ*, 389, 635
- Verner, E., Bruhweiler, F. & Gull, T. 2005, *ApJ*, 624, 973
- Whitelock, P. A., Feast, M. W., Marang, F., & Breedt, E. 2004, *MNRAS*, 352, 447 (astro-ph/0404513)
- Williams, P. M., van der Hucht, K. A., Pollock, A. M. T., Florkowski, D. R., van der Woerd, H., & Wamsteker, W. M. 1990, *MNRAS*, 243, 662

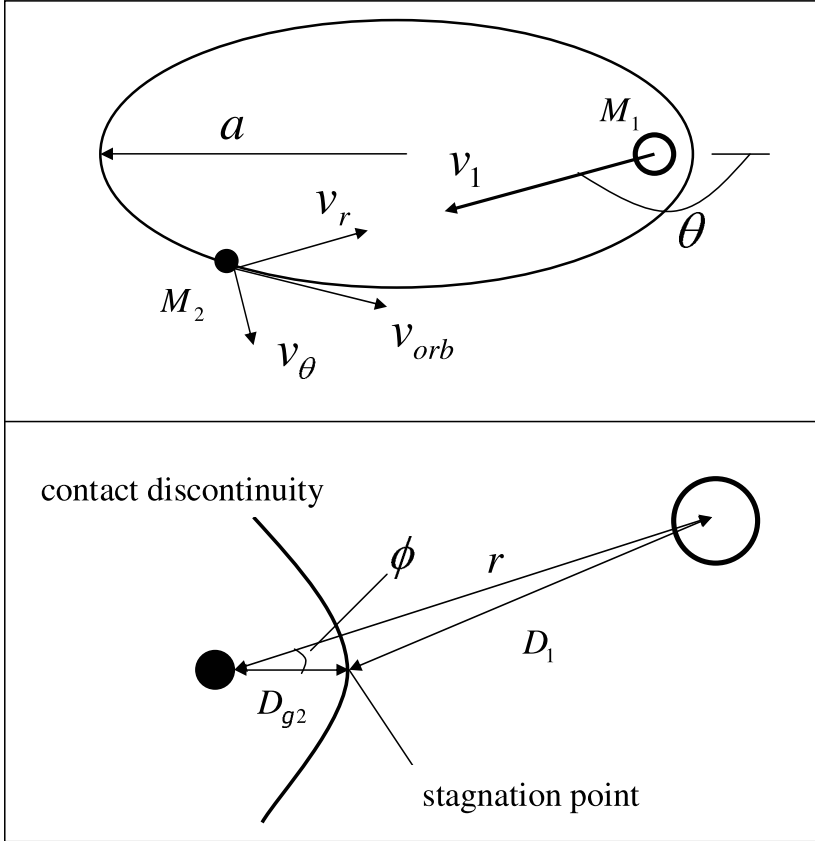


Fig. 1.— Upper panel: the orbit and relevant velocities in the rest frame of the primary star of mass M_1 . Drawn are the primary’s wind velocity v_1 , the two stars relative orbital velocity v_{orb} , and v_r and v_θ which are the radial and tangential components of v_{orb} , respectively. Lower panel: Geometrical definitions relevant to the flow near the stagnation point. The contact discontinuity is the surface where the two winds meet after they have passed the shock waves. The velocity directions in the lower panel are as in the upper panel (the secondary moves to the lower right). From Soker (2005b).

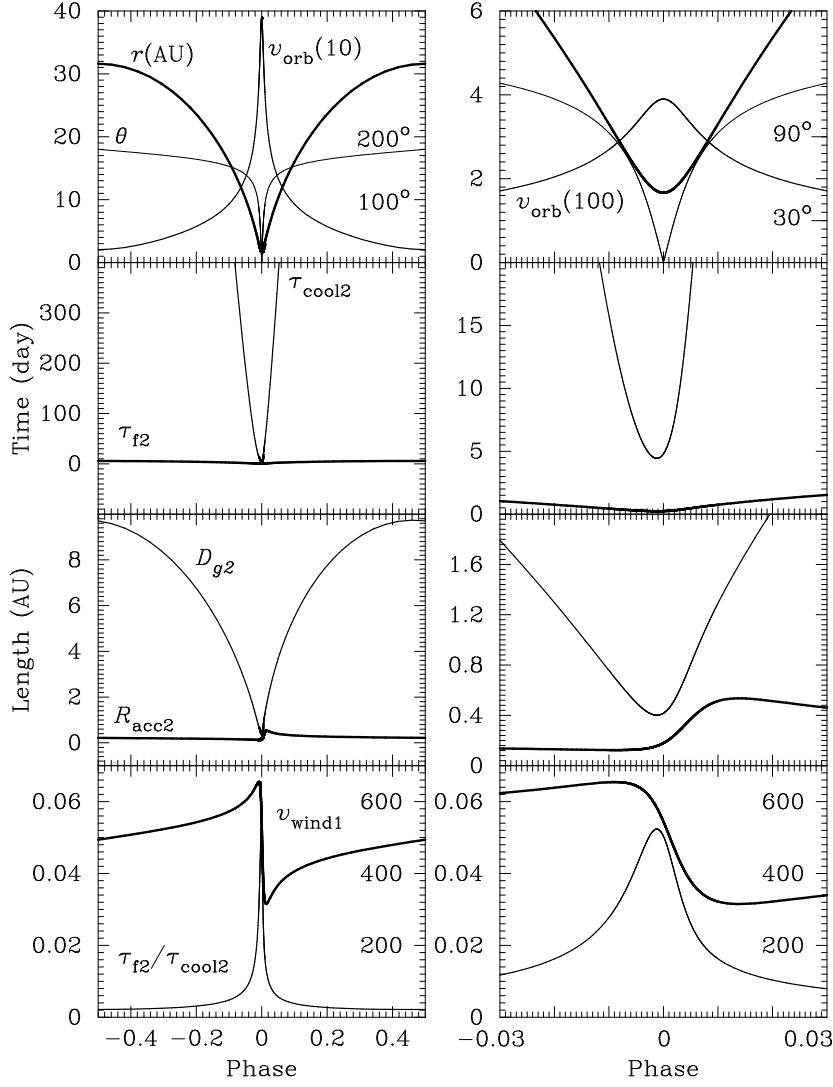


Fig. 2.— Several physical variables as function of orbital phase (phase zero is at periastron). The left column covers the entire orbit, while the column on the right covers the time just prior and after periastron. Upper row: The orbital separation r (in AU), and the relative orbital speed of the two stars v_{orb} (in 10 km s^{-1} on the left and 100 km s^{-1} on the right). The angle θ is the relative direction of the two stars as measured from periastron (scale on the right in degrees). Second row: The radiative cooling time of the shocked secondary’s wind near the stagnation point $\tau_{\text{cool}2}$ (upper line), and the typical time τ_{f2} for the shocked secondary wind to flow out of the winds interaction zone (lower line). Third row: the distance of the stagnation point from the secondary when the gravity of the secondary is included D_{g2} (upper line; see Figure 1), and the Bondi-Hoyle accretion radius of the secondary star $R_{\text{acc}2}$ (lower line). Lower row: The velocity of the primary wind relative to the stagnation point $v_{\text{wind}1}$ (thick line), and the ratio $\tau_{f2}/\tau_{\text{cool}2}$ (thin line). For more detail see Soker (2005b)

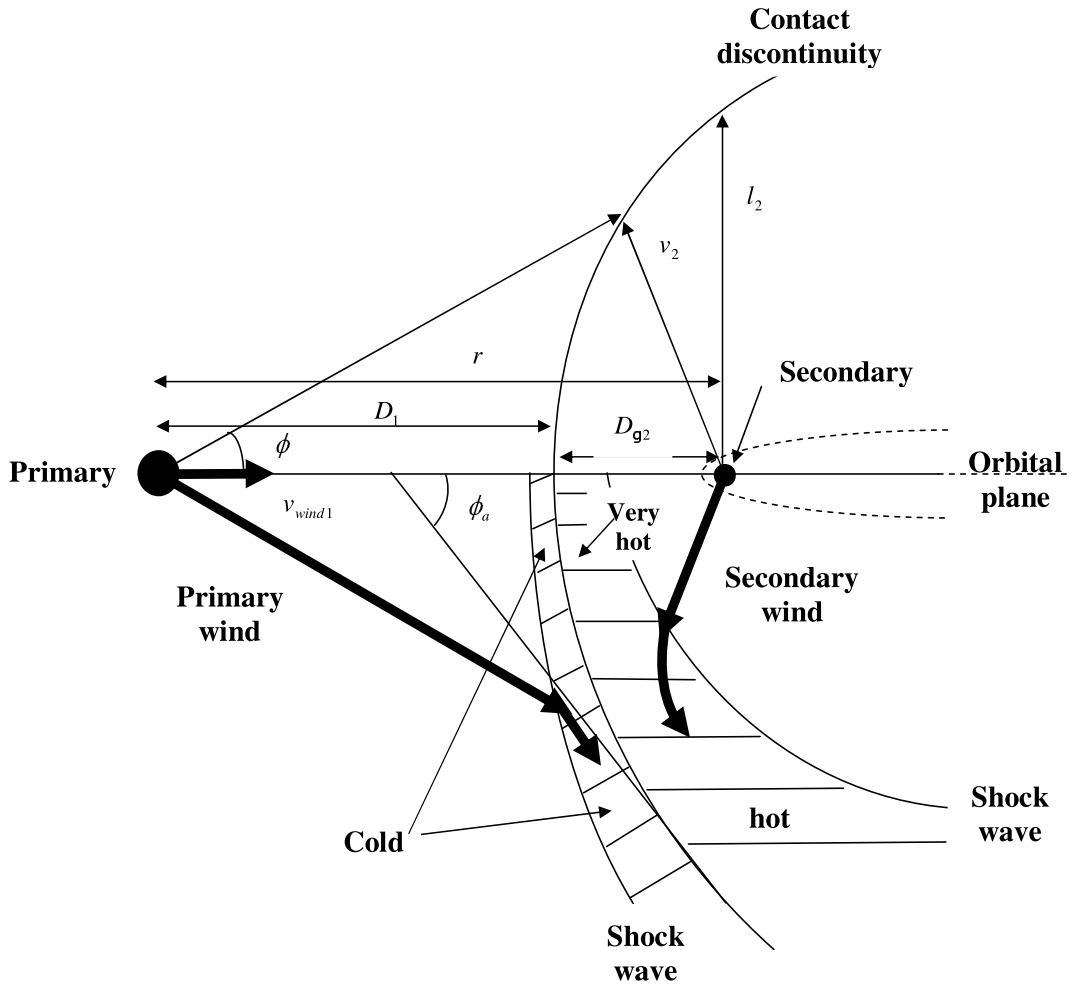


Fig. 3.— Schematic drawing of the collision region of two stellar winds and definition of several quantities. The two thick lines represent winds’ stream lines. The two shock waves are drawn only in the lower half. The post-shock regions of the two winds are hatched. The dashed line shows the accretion column which exists, according to the proposed model, only for $\sim 70 - 80$ days during the accretion period which corresponds to the X-ray minimum. This region is enlarged for this accretion period in figure 7.

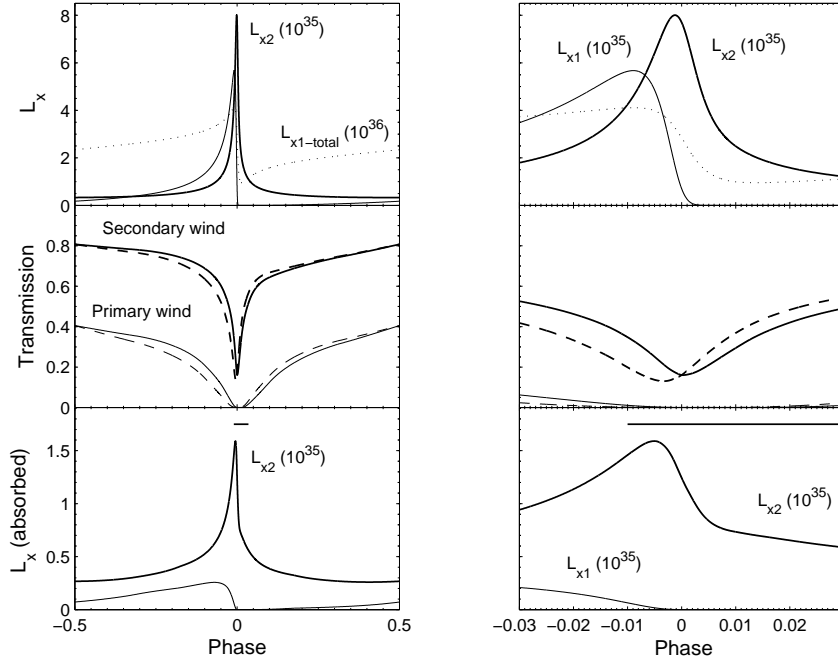


Fig. 4.— The X-ray luminosity outside the X-ray minimum. Upper row: the dotted line shows the intrinsic (absorption not included) luminosity of the shocked primary wind in the entire 0.01 – 10 keV band, in units of 10^{36} erg s^{-1} . The thin solid line shows the intrinsic luminosity of the shocked primary wind only in the 2 – 10 keV band L_{x1} (eq. 6), and the thick line shows the intrinsic luminosity of the shocked secondary wind only in the 2 – 10 keV band L_{x2} (eq. 8 with $k_2 = 2$), both in units of 10^{35} erg s^{-1} . Most of the contribution to L_{x1} is in the 2 – 3 keV band, explaining its large attenuation. Middle row: The X-ray transmission factor through the primary wind for the 2 – 10 keV band, calculated with XSPEC. Solid lines show the transmission using the column density calculated by equation (9) (or eq. 10), while the dashed lines show the transmission for an inclination $i = 42^\circ$ and periastron orientation $\omega = 180^\circ$ (equation 11); $k_g = 0.5$ in all cases. The two upper lines show the transmission of the X-ray emitted by the shocked secondary wind, while the two lower lines show the transmission of the X-ray emitted by the shocked primary wind. These lines emphasize the small difference between the two absorbing gas geometries considered here, and the high absorption of the X-ray emitted by the shocked primary wind. Lower row: The calculated X-ray luminosities of the shocked two winds in the 2 – 10 keV band when attenuation by equation (9) is included; thin and thick lines, respectively, represent the attenuated X-ray luminosities of the shocked primary and secondary winds. These quantities should be compared with observations outside the X-ray minimum. The horizontal line in each of the two panels in the lower row marks the time during which according to our model the secondary wind does not exist, or is highly suppressed. It spans the time starting a little before the minimum and ending a little after the minimum, phase -0.01 to 0.035 .

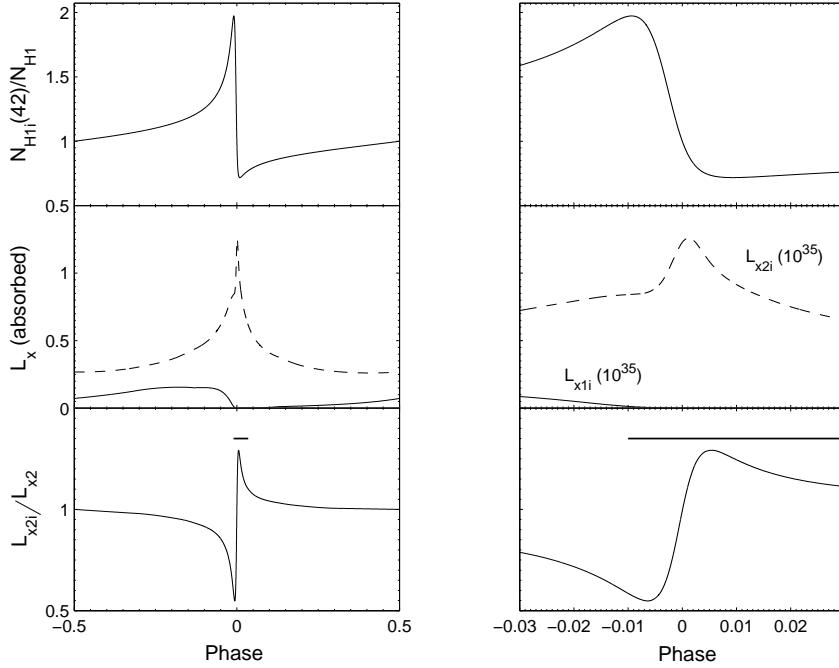


Fig. 5.— Upper row: the ratio $N_{H1i}(i = 42^\circ)/N_{H1}$, namely of the column densities in the two geometries considered here, where $N_{H1i}(i = 42^\circ)$ is from equation (11) and N_{H1} is from equation (9), or scaled in equation (10). Middle row: Like the lower row in Figure 4 but the observed X-ray luminosities L_{x2i} and L_{x1i} are calculated with attenuation by the column density $N_{H1i}(i = 42^\circ)$ with $k_g = 0.5$. Lower row: the ratio L_{x2i}/L_{x2} . This ratio shows that the differences between the two geometries considered here are small. The horizontal lines in the last row have the same meaning as in Figure 4

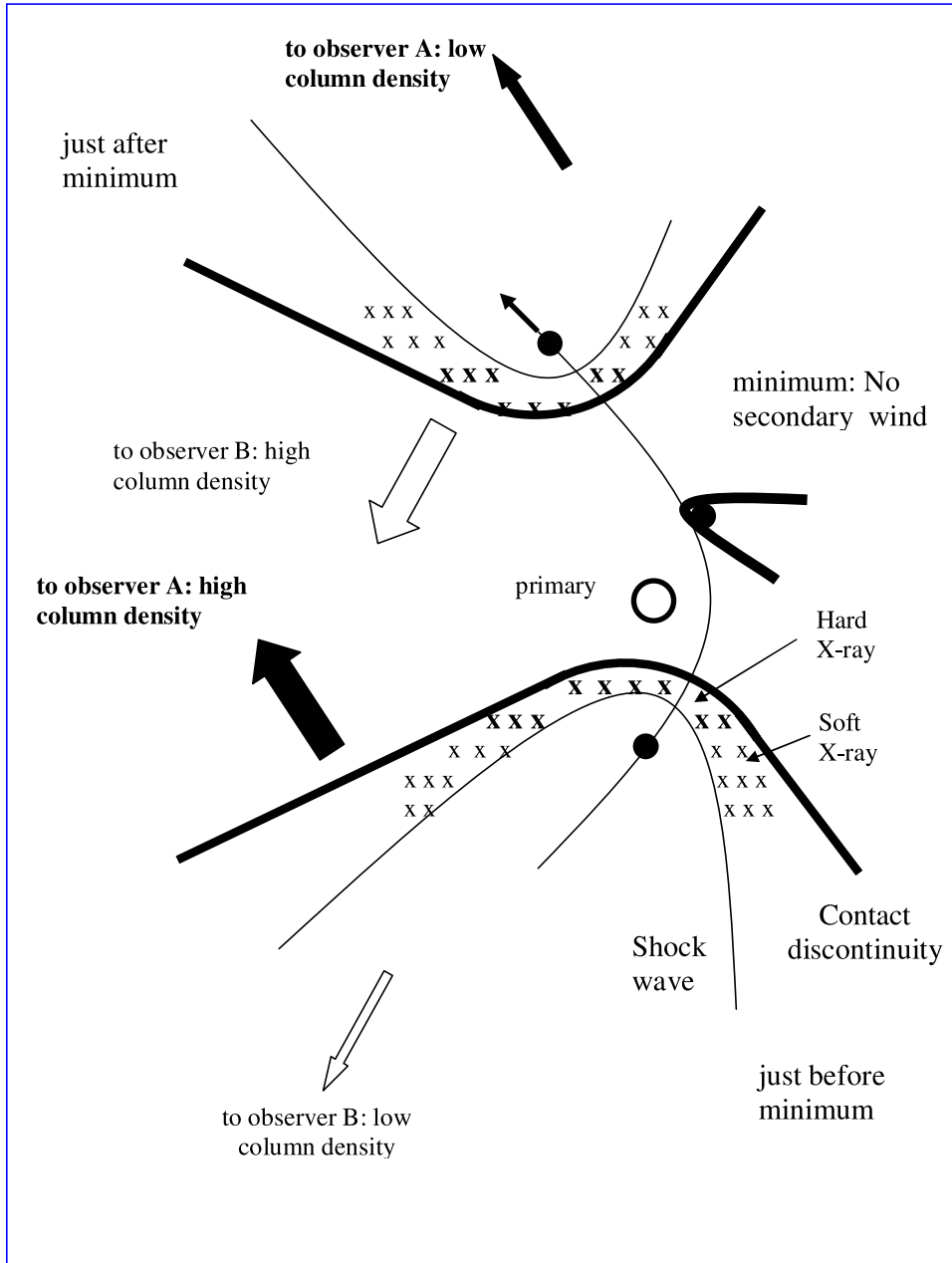


Fig. 6.— Schematic drawing (not for scaling and not the exact shock waves and contact discontinuity structures) of the flow structure at three epochs: Just before and after the X-ray minimum when the two wind exist, and during the X-ray minimum, when the secondary wind is assumed to be extinct. Note that according to our model the X-ray minimum is not symmetric about periastron. The shocked primary wind is marked by the thick arcs; the X-ray emitting shocked secondary wind is in the region marked by ‘x’s’; the open and filled circles mark the positions of the primary and secondary, respectively. Two possibilities for the orientation of the system are represented by the arrows (see text).

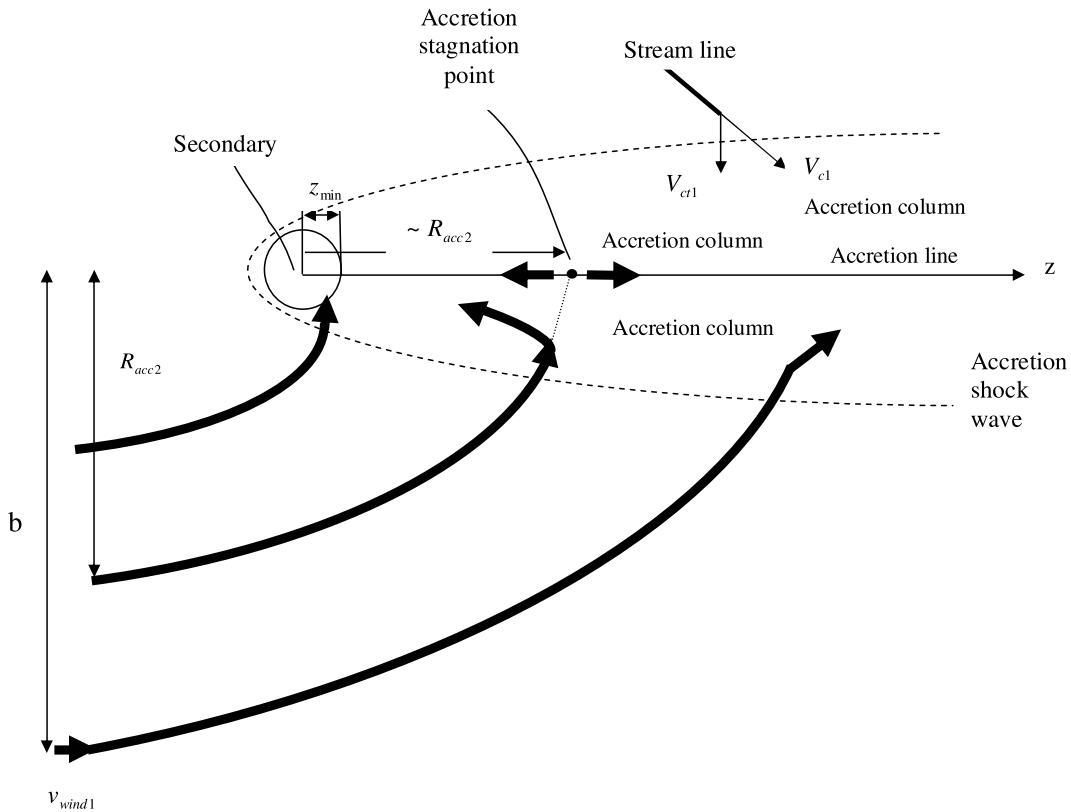


Fig. 7.— Schematic drawing of the isothermal high-Mach number Bondi-Hoyle-Lyttleton type accretion flow, and the definition of some quantities used in the text. We suggest that this type of accretion occurs during the X-ray minimum, and we further assume it shuts down the secondary wind. The stagnation point along the accretion line should not be confused with the stagnation point of the colliding winds.

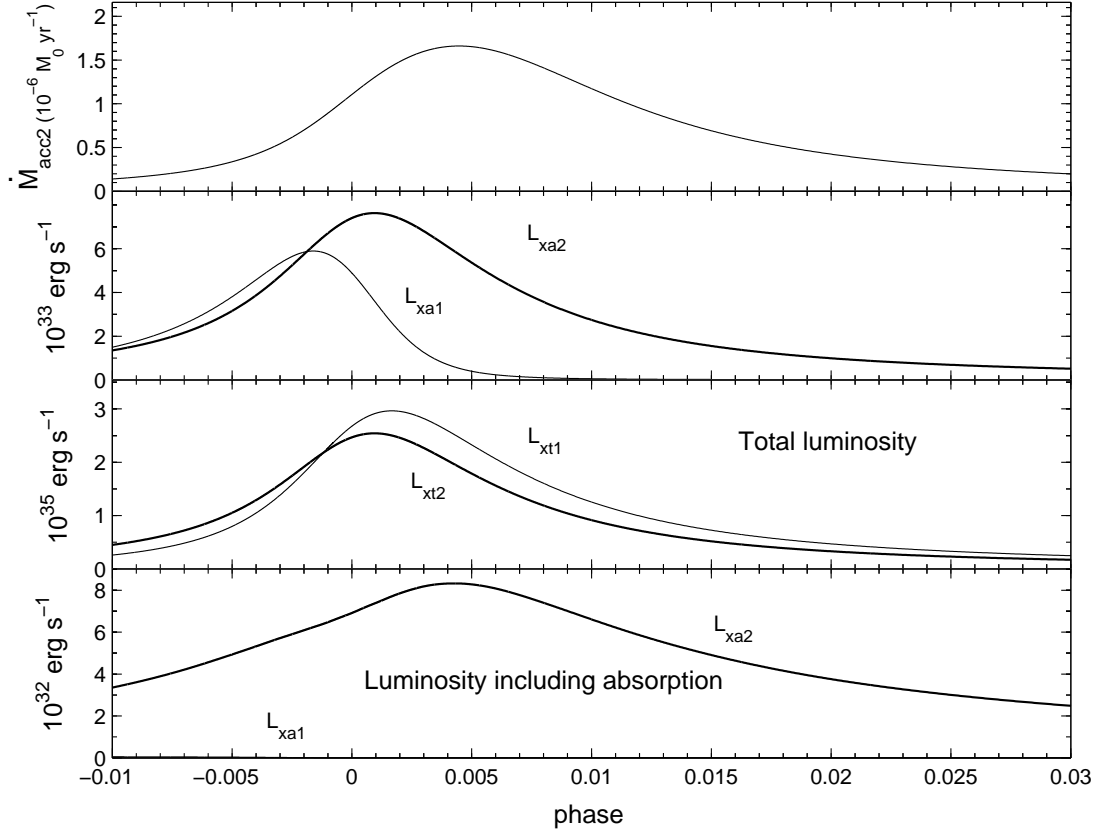


Fig. 8.— Quantities related to the X-rays emitted by primary wind material accreted onto the secondary during the X-ray minimum. Upper panel: The accretion rate \dot{M}_{acc2} (eq. 15). Second panel: The thick line shows the X-ray luminosity in the 2 – 10 keV band of material accreted by the secondary through the accretion column L_{xa1} (eq. 18). The thin line shows the X-ray luminosity in the 2 – 10 keV band of material accreted directly by the secondary L_{xa2} (20). Third panel: The total luminosity of the shocked accreted gas, namely, taking $F_{210} = 1$ in equations (18) and (20). Lower panel: The luminosities shown in the second panel but with absorption included. Note that the primary wind X-ray emission is completely absorbed.

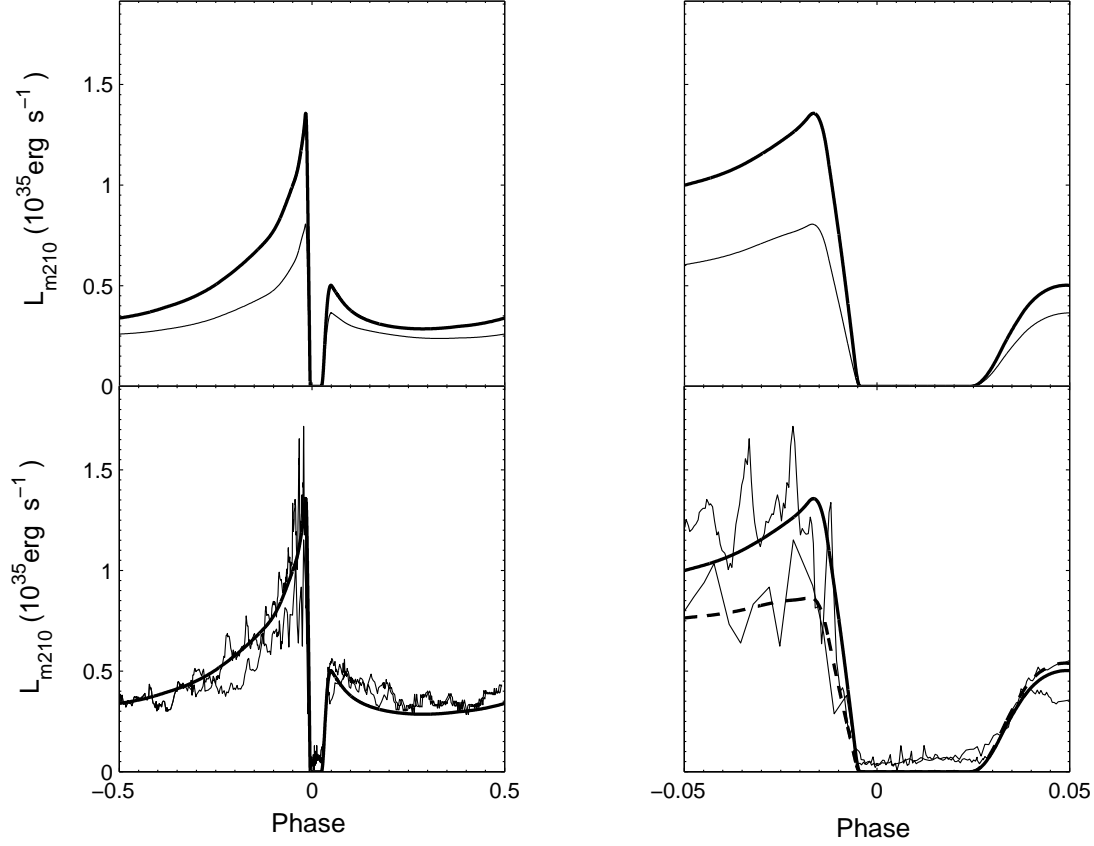


Fig. 9.— Upper row: The absorbed X-ray luminosity between 2 – 10 keV according to our model, namely, equation (25), but with absorption included and not considering the residual emission $L_{x\text{-res}}$. A value of $k_2 = 2$ is assumed in equation (7). The absorbing column density is according to equation (10), with $k_g = 0.5$ (thick line) and $k_g = 1$ (thin line). Lower row: The model absorbed X-ray luminosity with $k_g = 0.5$ (thick line), and the observed X-ray luminosity from Corcoran (2005) in the 2 – 10 keV band for a period covering two X-ray minima (two thin lines). The dashed line in the right lower panel shows the X-ray emission for $\omega = 180^\circ$ and $i = 42^\circ$ (see eq. 11).